fluids

MDPI

Article

Linear Stability Analysis on Flow-Induced Vibration of an Elastically Mounted Rotating Cylinder

Jianfeng Lu [1,2], Zhiyu Zhang [1,2] and Xing Zhang [1,2,*]

[1] The State Key Laboratory of Nonlinear Mechanics, Institute of Mechanics, Chinese Academy of Sciences, Beijing 100190, China; lujianfeng@imech.ac.cn (J.L.); zhangzhiyu@imech.ac.cn (Z.Z.)
[2] School of Engineering Science, University of Chinese Academy of Sciences, Beijing 100049, China
* Correspondence: zhangx@lnm.imech.ac.cn

Abstract: In this paper, we present a linear stability analysis on flow-induced vibration of an elastically mounted cylinder subjected to forced rotation. Four series of cases, with different combinations of degrees of freedoms in oscillation and Reynolds number are investigated. For each series of cases, a wide range of reduced velocity at various rotation rates are considered. The variations of growth and frequency with reduced velocity for the leading modes are presented. Some phenomena observed in previous numerical studies are interpreted by using the results of linear stability analysis. The supressing of vortex shedding at moderate rotation rate is explained by the absence of unstable fluid mode. The amplitude enhancement in high range of rotaton rate is explained by the emergence of unstable elastic mode. The stability properties of the leading modes provide some new insight into the influences of forced rotation on flow-induced vibration. The results of the current study have important implications in the design of offshore structures and energy-havesting devices.

Keywords: linear stability analysis; flow-induced vibration; elastically mounted cylinder; forced rotation; fluid mode; elastic mode

Academic Editor: Fang-Bao Tian

Received: 2 February 2025
Revised: 17 February 2025
Accepted: 18 February 2025
Published: 21 February 2025

Citation: Lu, J.; Zhang, Z.; Zhang, X. Linear Stability Analysis on Flow-Induced Vibration of an Elastically Mounted Rotating Cylinder. *Fluids* **2025**, *10*, 56. https://doi.org/10.3390/fluids10030056

1. Introduction

Flow-induced vibration (FIV) is a common phenomenon in nature and is also frequently encountered in civil, offshore, and nuclear engineering structures. The occurrence of FIV can lead to fatigue damage and safety issues [1]. On the other hand, FIV can also be utilized to harvest hydrokinetic and wind energy from the environment [2]. The prevention and exploitation of FIV in engineering applications have motivated the study of this phenomenon.

An elastically mounted circular cylinder that is free to oscillate in the cross-flow direction is the canonical FIV model. The first type of FIV behavior in this model is termed 'vortex-induced vibration (VIV)'. The oscillation amplitude is greatly amplified when the vortex shedding frequency locks onto the natural frequency. In the classical hydroelasticity theory, the frequency lock-in in VIV is interpreted as a resonance phenomenon in forced-vibration systems [3]. Recently, by using linear stability analysis (LSA), a second excitation mechanism in VIV, namely, the flutter-induced mechanism, has been identified. Unlike the resonance-related mechanism (which is rooted in the instability of a fluid mode), the flutter-induced mechanism is rooted in the instability of a structural (elastic) mode [4].

For objects with non-axially symmetric cross-sections (such as a square or a D-shaped cylinder), a second type of FIV behavior termed 'galloping' may appear. Such phenomenon

is characterized by a low-frequency oscillation, the amplitude of which increases unboundedly with the reduced velocity. Unlike VIV, galloping is caused by asymmetric pressure distribution due to the effect of instantaneous angle of attack. The synchronization between body oscillation and vortex formation is not involved in galloping [3].

FIV of an elastically mounted cylinder with forced rotation has attracted some attention recently [5–8]. Such configuration has practical application in offshore engineering where drilling risers without casing may be exposed to ocean currents. The possible enhancement of oscillating amplitude due to imposed rotation also has some implications in energy-harvesting devices. A series of computational studies on such configurations at low Reynolds numbers of the order $O(10) - O(10^2)$ were conducted. Among these works, some were concerned with 1-DOF oscillations of a rotating cylinder [9–11]. Bourguet & Lo Jacono [9] investigated into the cross-flow flow-induced vibrations of a rotating cylinder, and they found significant enhancement in oscillation amplitudes of the rotating cylinders in comparison with the non-rotating ones. They also confirmed that the free oscillation of a rotating cylinder were induced by wake-body synchronization mechanism (similar to that found in non-rotating cylinders). In a subsequent study by Bourguet & Lo Jacono [10], in-line flow-induced vibrations of a rotating cylinder were explored. In the entire range of rotation rate (ratio of speed on the cylinder surface and that of the incoming flow), two vibration regimes which were interposed by a non-vibration regime, were identified. In the vibration regime at a low rotation rate, the oscillation was induced by the wake-synchronization mechanism. In the vibration regime at a high rotation rate, where the amplitude increased unboundedly with reduced velocity, the FIV behavior was very similar to that in the galloping phenomenon observed in a square (or D-shaped) cylinder. The study by Bourguet [11] bridged the gap between these two works by considering rotating cylinders which were free to oscillate in an arbitrary direction.

2-DOF vibrations of a rotating cylinder were considered in some other references [8,12–15]. In the study by Bourguet [12], it was found that if the cylinder was free to oscillate in both the cross-flow and the in-line directions, the responses may differ significantly from its 1-DOF counterparts. Flow-induced vibrations were found to exist in the entire range of rotation rate (from 0 to 5.5). In the work of Zhao et al. [8], the responses of 1-DOF and 2-DOF oscillators were compared, and the roles of pressure and viscous forces in exciting and damping the vibrations were analyzed. Sahu et al. [13] discovered multiple lock-in regimes in a 2-DOF oscillator at various rotation rates. Each lock-in regime was associated with a different wake pattern. Amini et al. [14] studied the effects of mass ratio on oscillation amplitude and heat transfer. In a more recent work by Bourguet [15], focus was placed on how the forced rotation affected subcritical-*Re* VIV of a rotating cylinder, which was down to very low Reynolds numbers. It was found that, at high rotation rates, the vibration region considerably expanded, and the amplitude was greatly enhanced. In addition, a transition from VIV to galloping was also observed at a sufficiently high rotation rate.

In almost all aforementioned references, numerical investigations were conducted by solving nonlinear (Navier–Stokes) equations. The only exception was the one by Sahu et al. [13] where a linear stability analysis (LSA) was also performed. The LSA results revealed that FIV can be induced by instabilities in the fluid, elastic, or coupled fluid–elastic modes, depending on the values of rotation rate and reduced velocity.

The new contribution of the current study is a systematic investigation on how forced rotation affects FIV behaviors by using LSA. More specifically, we considered 1-DOF (cross-flow and in-line) and 2-DOF oscillators, which were explored using nonlinear simulations by Bourguet and co-workers [9,10,12,15]. The LSA results are expected to provide some new insights into the mechanisms behind distinct FIV behaviors at different ranges of

rotation rate. These important information are expected to be helpful in guiding the design of offshore structures and energy-harvesting devices.

The arrangement of rest of this paper is as follows. Section 2 presents the physical model and governing equations. Section 3 presents a brief introduction on the numerical methods for performing LSA. Section 4 presents the results and discussion. Finally, some concluding remarks are provided in Section 5.

2. Physical Model and Governing Equations

In this paper, we consider a rigid circular cylinder that is elastically mounted and immersed in a two-dimensional incompressible viscous flow. A schematic representation of the physical model is shown in Figure 1. The cylinder is free to oscillate in the in-line or cross-flow direction (or both). The cylinder has a diameter of D and is forced to rotate at an angular velocity of Ω.

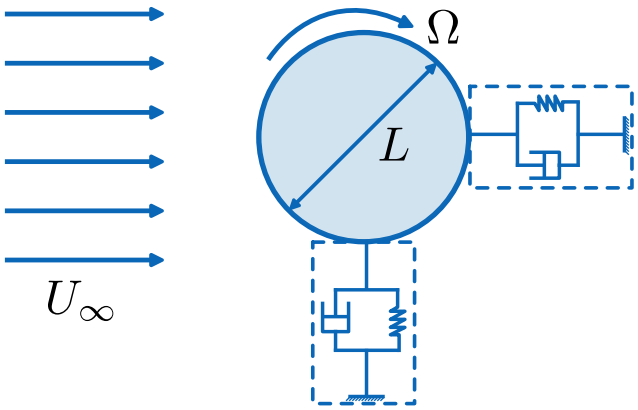

Figure 1. Schematic diagram of the physical model.

The flow is assumed to be laminar and is governed by incompressible Navier–Stokes equations, which can be written in a dimensionless form as follows:

$$\frac{\partial \boldsymbol{u}}{\partial t} + (\boldsymbol{u} \cdot \nabla)\boldsymbol{u} = -\nabla p + \frac{1}{Re}\nabla^2 \boldsymbol{u} + \boldsymbol{f}, \tag{1a}$$

$$\nabla \cdot \boldsymbol{u} = 0, \tag{1b}$$

where $\boldsymbol{u}$ is the velocity vector and p is the pressure. $\boldsymbol{f}$ is the body-force term which represents the interaction between the flow and the immersed object. In the immersed boundary method used to solve the Navier–Stokes equations, this term can be implicitly determined by enforcing no-slip condition on the surface of the object.

The oscillating motions of the cylinder are governed by Newton's second law, which can be written in a dimensionless form as follows:

$$\ddot{x} + 2\xi\left(\frac{2\pi}{U^*}\right)\dot{x} + \left(\frac{2\pi}{U^*}\right)^2 x = \frac{F_x}{m^*} = \frac{C_D}{2m^*}, \tag{2a}$$

$$\ddot{y} + 2\xi\left(\frac{2\pi}{U^*}\right)\dot{y} + \left(\frac{2\pi}{U^*}\right)^2 y = \frac{F_y}{m^*} = \frac{C_L}{2m^*}, \tag{2b}$$

where x and y denote the horizontal and vertical positions of the cylinder center. U^* is the reduced velocity, ξ is the dimensionless damping coefficient, and m^* is the mass ratio. C_L and C_D are the lift and drag coefficients which are defined as $C_L = F_y/(\rho_f U_\infty^2 L)$ and $C_D = F_x/(\rho_f U_\infty^2 L)$, where F_y and F_x are the vertical and horizontal components of the resultant hydrodynamic force exerted on the cylinder. In the framework of immersed

boundary method for solving Navier–Stokes equations, this hydrodynamic force can be computed by using the body-force $\boldsymbol{f}$.

The inflow which comes from left to right has a uniform velocity of U_∞. The reference length and time used in the nondimensionalization are L and L/U_∞, respectively. The dynamic behavior of the FIV system is determined by five dimensionless parameters, namely, Reynolds number Re, reduced velocity U^*, mass ratio m^*, dimensionless damping coefficient ξ, and rotation rate α. The definitions of these parameters are as follows:

$$Re = \frac{LU_\infty}{\nu}, \tag{3a}$$

$$U^* = \frac{U_\infty}{f_n L} = \frac{U_\infty}{L} 2\pi \sqrt{\frac{m_s}{k}}, \tag{3b}$$

$$m^* = \frac{\rho_s}{\rho_f}, \tag{3c}$$

$$\xi = \frac{\kappa}{2\sqrt{km_s}}, \tag{3d}$$

$$\alpha = \frac{2\Omega}{U_\infty L}. \tag{3e}$$

Here, ν is the kinematic viscosity of the fluid, m_s is the mass of the cylinder, and f_n is the natural frequency of the spring-mass system in vacuum. ρ_f and ρ_s are the densities of the fluid and the cylinders, respectively. κ and k are the damping coefficient and stiffness coefficient, respectively. In this paper, we only consider cases with no structural damping, and thus $\xi = \kappa = 0$. Such setting facilitates higher oscillation amplitudes in simulation and is often used when the effect of structural damping is not the main concern.

3. Numerical Methods

In this study, we conduct LSA by using the linear stability solver developed in Zhang et al. [16]. It utilizes a direct-forcing immersed boundary method based on stream-function formulation to solve the linearized equations of the FIV system. The immersed boundary method aforementioned was first proposed by Wang & Zhang [17] for solving incompressible Navier–Stokes equations with stationary and moving boundaries.

The state variable of the FIV system can be written as $\boldsymbol{q} = [s, \mathbf{V}, \mathbf{X}, \mathbf{F}]^T$. Here, s is the stream function, which is the primary unknown in the discretized stream-function formulation of Navier–Stokes equations. $\mathbf{V}$ is the velocity of the cylinder center, i.e., $\mathbf{V} = [\dot{x}, \dot{y}]^T$. $\mathbf{X}$ represents the position vectors of the Lagrangian points on the cylinder surface. $\mathbf{F}$ represents the Lagrangian forces at these points.

The state variable can be described as the summation of base and perturbation variables, i.e., $\boldsymbol{q} = \boldsymbol{q}_b + \boldsymbol{q}'$. The subscript $()_b$ indicates the base variable that can be obtained by solving steady Navier–Stokes equations with the cylinder placed at its equilibrium position. The prime symbol represents the perturbation variable. By linearizing the governing Equations (1) and (2) around the base state, we can derive the linearized equations for the perturbation variable of the FIV system, i.e.,

$$\boldsymbol{B}\frac{\partial \boldsymbol{q}'}{\partial t} = \boldsymbol{A}(\boldsymbol{q}_b)\boldsymbol{q}'. \tag{4}$$

Here, $\boldsymbol{A}$ and $\boldsymbol{B}$ are two matrices that are constructed based on operators involved in discretizing the linearized equations. By using the normal-mode assumption $\boldsymbol{q}' = \hat{\boldsymbol{q}}e^{\lambda t}$ (where λ is the circular frequency), Equation (4) can be reformulated as a generalized eigenvalue problem: $\lambda \boldsymbol{B}\hat{\boldsymbol{q}} = \boldsymbol{A}\hat{\boldsymbol{q}}$. We utilize the shift–invert iteration method provided in software

packages PETSc 3.20.0 and SLEPc 3.20.0 to solve this generalized eigenvalue problem. The linear stability solver has been thoroughly validated by computing eigenvalues and eigenmodes for the FIV system of flow past an elastically mounted cylinder [16]. In the current study, the residual tolerances on eigenvalue and eigenvector are set to 1.0×10^{-10}.

The real part of eigenvalue λ (i.e., λ_r) represents the growth (or decay) rate of the eigenmode. The eigenmode is stable, neutral, or unstable, if the eigenvalue is negative, zero, or positive, respectively. The imaginary part of eigenvalue λ (i.e., λ_i) represents the oscillating frequency of the eigenmode.

4. Results and Discussion

4.1. Control Parameters and Numerical Settings

LSA is performed on four series of cases. The physical parameters for these cases are listed in Table 1. In each series, the Reynolds number is fixed, while the rotation rate and reduced velocity may vary. The value of mass ratio m^* is set to 10.0 for all cases in this study. This value is chosen to be the same as that in the nonlinear simulations by Bourguet and co-authors [9,10,12,15].

Table 1. Values of control parameters in this study.

Series	*Re*	DOFs	α	U^*
1	100	1 (in-line)	[0.0, 1.0, 2.5, 3.0, 4.0]	4.0–30.0
2	100	1 (cross-flow)	[0.0, 1.0, 2.0, 3.0, 4.0]	4.0–30.0
3	100	2 (both)	[0.0, 1.0, 2.1, 3.0, 4.0]	4.0–30.0
4	30	2 (both)	[0.0, 1.0, 2.0, 3.0, 4.0]	4.0–30.0

Series 1 represents the scenario of in-line oscillation at a supercritical Reynolds number [10]. Series 2 represents the scenario of cross-flow oscillation at a supercritical Reynolds number [9]. Series 3 and series 4 represent the scenarios of 2-DOF oscillations at a supercritical [12] and a subcritical Reynolds number [15], respectively. Here, the critical Reynolds number (which is roughly 47) refers to the one for onset of vortex shedding in flow past a rigidly mounted non-rotating cylinder.

The parameter range of this study is carefully chosen such that the flow is strictly two-dimensional within almost the entire range. Three-dimensionality may develop in a very narrow parameter range with a high Re number and high rotation rate. For cases in such parameter range, the nonlinear simulation results mentioned here are referred to as those obtained by conducting 2D simulations. It should also be noted that, even for cases in which the transition from 2D to 3D may occur, the structure responses are barely affected by the transition.

A non-uniform Cartesian mesh on a computational domain of $[80D \times 56D]$ is used to perform linear stability analysis. The mesh is stretched in such a way that the minimum grid spacing of $0.02D$ is uniformly distributed in a small region of $[10D \times 4D]$ around the cylinder, while the maximum grid spacing of $0.55D$ is attained near the domain boundaries.

To ensure that the mesh resolution is fine enough, and the domain size is sufficiently large for obtaining accurate solutions, convergence tests are conducted, and the results are presented in Appendix A.

4.2. In-Line Oscillation at a Supercritical Reynolds Number (Series 1)

Some results for series 1 from the nonlinear simulation of Bourguet & Lo Jacono [10] are summarized in Figure 2. Figure 2a shows the vibration and non-vibration regions in the space of (U^*, α). It is seen that there exist two vibration regions at the low and high ranges of rotation rate, respectively. These two vibration regions are separated by a non-vibration

region (without flow unsteadiness) at the intermediate range of rotation rate. Figure 2b shows the amplitude of oscillation as a function of U^* at various rotation rates. For the vibration region in the low range of rotation rate, amplitudes are very small and the curves are bell-shaped. For the vibration region in the high range of rotation rate, amplitudes are much larger and tend to increase unboundedly with U^*. This is the typical behavior of galloping responses that are found in FIV of non-axisymmetic objects. The cases selected for conducting LSA are denoted as dots in Figure 2a. Different colors are assigned to these dots depending on stability properties of the leading modes. It is evident that the critical values of U^* for onset of oscillation in the high range of rotation rate can be predicted by using stability properties of the leading modes.

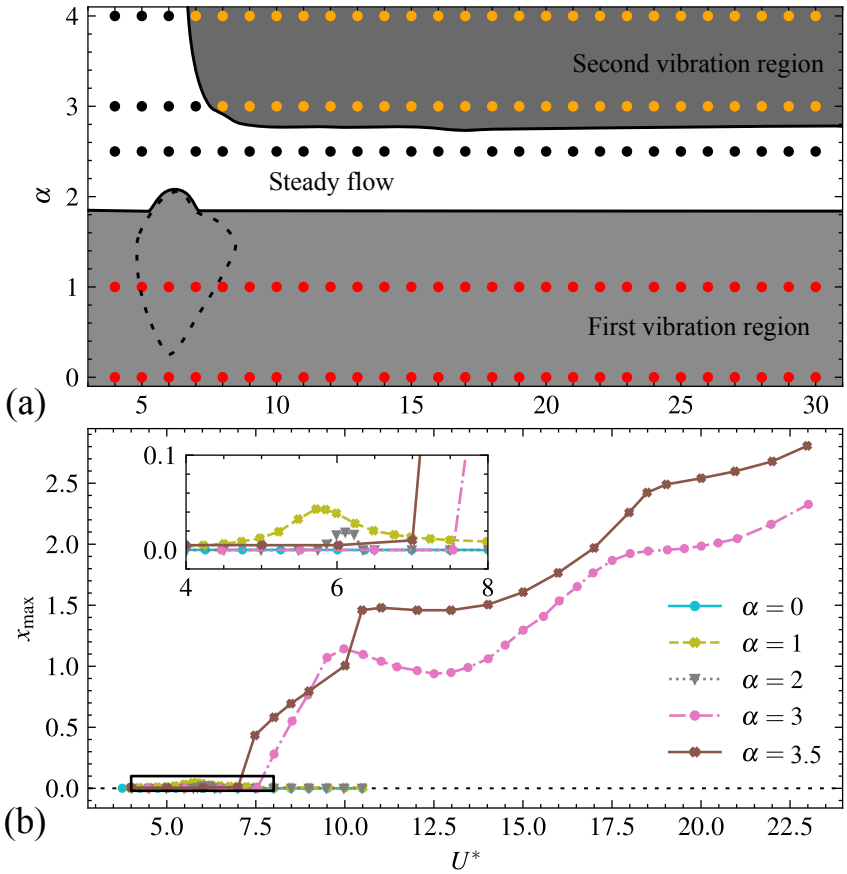

Figure 2. Results from nonlinear simulation for FIV of an in-line oscillator at $Re = 100$ (series 1): (**a**) vibration region and non-vibration regions in (U^*, α). The lower vibration region is represented in light grey. In this region, the area in which the amplitude is large than $0.01D$ is enclosed by a dashed line. The upper vibration region is represented in dark gray. The black dots represent cases without unstable mode(s). The red and orange dots represent cases with one unstable FM mode and one unstable EM mode, respectively. (**b**) The amplitude of oscillation as a function of U^*. The boundary lines in (**a**) and curves in (**b**) are re-plotted by using digitized data extracted from Bourguet & Lo Jacono [10].

Figure 3 shows the variations in growth rate (λ_r) and non-dimensional frequency (f^*) with reduced velocity (U^*) for one (or two) leading mode(s) obtained at $\alpha = 0, 1.0, 3.0$. At ($\alpha = 0$) (which represents the non-rotating case), it is evident that one leading mode remains unstable in the entire range of U^*. We refer to this mode as the fluid mode (FM), since its frequency is nearly invariant with varying U^*. The other leading mode (which is always stable) is referred to as the elastic mode (EM), since its frequency varies inversely with U^*. At $\alpha = 1.0$, the results are very similar to those for $\alpha = 0$. In other words, the LSA results are barely affected by the imposed rotation. At $\alpha = 2.5$, it is found that no unstable

leading modes exist in the entire range of U^*. This is consistent with the result of nonlinear simulation in which cylinder oscillation and flow unsteadiness are completely inhibited. The growth rate and dimensionless frequency of the leading modes are not shown here for brevity. At $\alpha = 3.0$, one leading mode, which is unstable when $U^* > 7.5$, is identified as an EM mode. The critical value of $U^* = 7.5$ is close to the value for onset of oscillation in nonlinear simulation (see Figure 2a). The fact that the EM mode remains unstable at the high limit of U^* can be used to rationalize the unbounded increase in amplitude with increasing U^*.

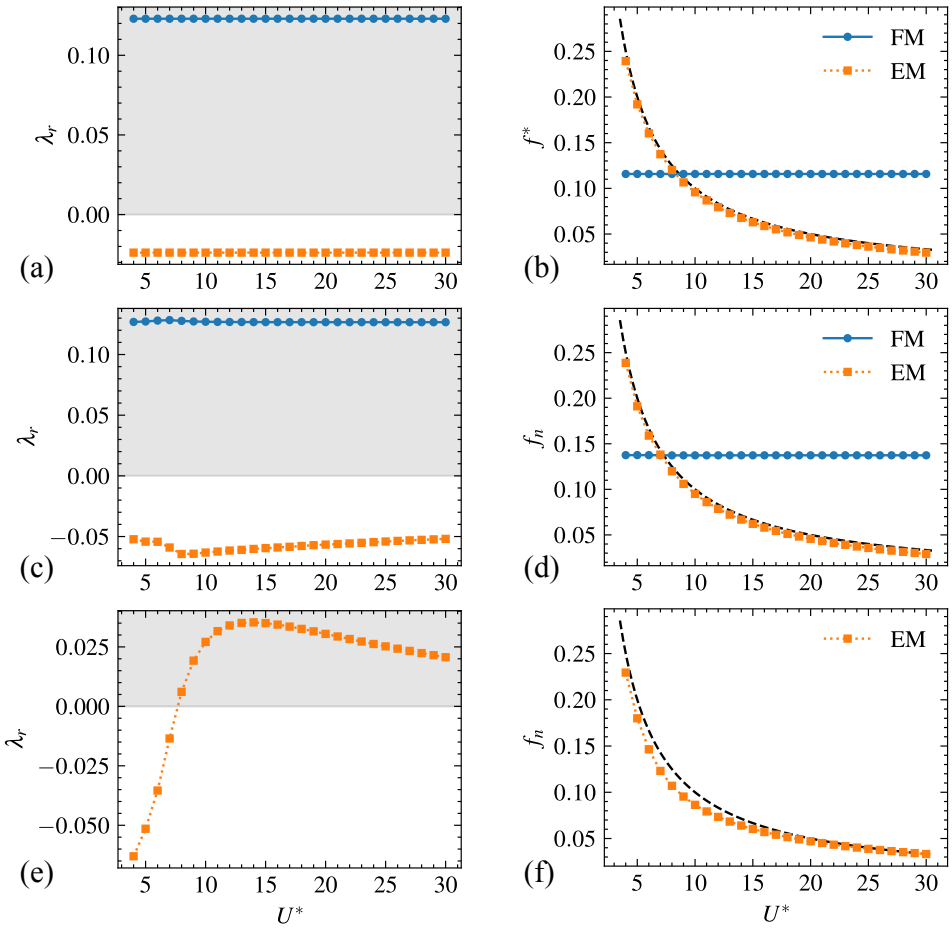

Figure 3. LSA results for FIV of an in-line oscillator at $Re = 100$ (series 1): growth gate λ_r and dimensionless frequency $f^* = \lambda_i/(2\pi)$ as a function of U^* at $\alpha = 0$ (**a**,**b**); $\alpha = 1.0$ (**c**,**d**); $\alpha = 3.0$ (**e**,**f**). The unstable regions (with a positive growth gate) in the (**left panel**) are shaded in gray. The (dimensionless) natural frequencies as a function of U^* are shown as dashed lines in the (**right panel**).

Figure 4 shows the structures (vorticity fields) of the FM and EM modes for some cases at $\alpha = 1.0$ and $\alpha = 3.0$. It is seen that the structures of FM modes are not significantly affected by varying U^*. These structures are similar to those observed in flow past a rigidly mounted non-rotating cylinder. On the other hand, the structures of EM modes strongly depend on the value of U^*. The spacing between adjacent lobes appears to increase in length in the streamwise direction with increasing U^*. The increase in spacing between vorticity lobes for the EM modes is consistent with the reduction in frequency. This trend was reported previously in the study by Sahu et al. [13].

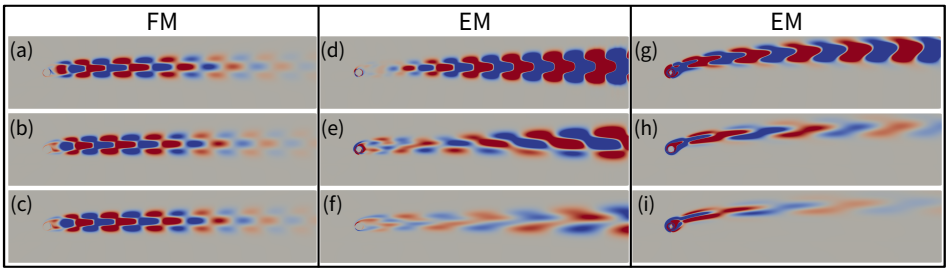

Figure 4. Mode structures for some cases in series 1: vorticity fields of FM modes (**left panel**) and EM modes (**middle panel**) for $\alpha = 1.0$, and EM modes for $\alpha = 3.0$ (**right panel**). Frames (**a**,**d**,**g**), (**b**,**e**,**h**), and (**c**,**f**,**i**) are for $U^* = 6.0, 10.0, 15.0$, respectively. The ranges of vorticity are $[-5 \times 10^{-3},\ 5 \times 10^{-3}]$ for (**a**–**c**), $[-5 \times 10^{-4},\ 5 \times 10^{-4}]$ for (**d**–**f**), and $[-10^{-5},\ 10^{-5}]$ for (**g**–**i**). The incoming flow is from left to right.

4.3. Cross-Flow Oscillation at a Supercritical Reynolds Number (Series 2)

Some results for series 2 from the nonlinear simulation of Bourguet & Lo Jacono [9] are summarized in Figure 5. Figure 5a shows the vibration and non-vibration regions in the space of $(U^*,\ \alpha)$. Dark gray represents the region of high-amplitude oscillation, which extends from $\alpha = 0$ to $\alpha = 3.75$. Light gray represents the region of low-amplitude oscillation (with flow unsteadiness). The cases selected for conducting LSA are denoted as dots in different colors, depending on the stability properties of the leading modes. It is seen that the boundary lines between different regions in Figure 5a can be predicted by using stability properties of the leading modes. Figure 5b shows the amplitude of oscillation as a function of U^* at various rotation rates. At $\alpha = 0$, the response curve is bell-shaped. At $\alpha = 1.0$, the shape of response curve is very similar to that of $\alpha = 0$. The amplitude of oscillation slightly increases, and the range of U^* for high-amplitude oscillation slightly expands and shifts towards high U^* values. The curves of such shape is a hallmark of the VIV response. At $\alpha = 2.0$ and $\alpha = 3.0$, the amplitudes further increase, and the ranges of U^* for high-amplitude oscillation significantly expand. The shapes of these curves are markedly dissimilar to those of the curves for $\alpha = 0$ and $\alpha = 1.0$. At $\alpha = 4.0$, the oscillation is completely suppressed, and the amplitude is reduced to zero.

Figure 6 shows the variations in growth rate (λ_r) and non-dimensional frequency (f^*) with reduced velocity (U^*) for the leading mode(s) calculated at $\alpha = 0, 1.0, 2.0$. At $\alpha = 0$, the FM mode is found to be unstable over the entire range of U^*, while the EM mode is found to be unstable in the range of $5.0 \leq U^* \leq 10.0$. At $\alpha = 1.0$, the stability properties of the two leading modes are very similar to those for $\alpha = 0$. At these two rotation rates, the coexistence of unstable FM and EM modes in certain range of U^* signifies the resonance (synchronization) between flow unsteadiness and cylinder oscillation. This range of U^* roughly coincides with the range for high-amplitude oscillation shown in Figure 5a. At $\alpha = 2.0$, the FM mode becomes stable in the entire range of U^*, while the EM mode is found to be unstable in the range of $6.0 \leq U^* \leq 17.0$. This range of U^* also coincides with the range for high-amplitude oscillation shown in Figure 5a. At $\alpha = 4$, it is found that no unstable leading modes exist in the entire range of U^*. This finding is consistent with the result of nonlinear simulation, in which the amplitude is reduced to zero. The growth rate and frequency of the leading modes are not shown here for brevity.

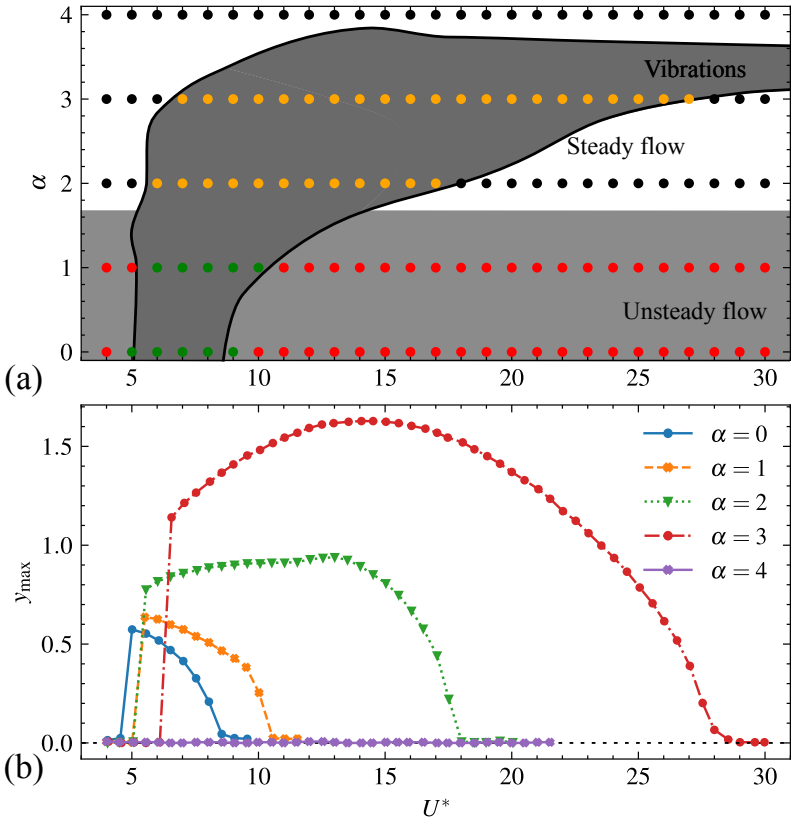

Figure 5. Results from nonlinear simulation for the FIV of a cross-flow oscillator at $Re = 100$ (series 2): (**a**) vibration and non-vibration regions in space of (U^*, α). The vibration region where the amplitude is larger than 0.05D is represented in dark gray. The vibration region with low amplitude (and flow unsteadiness) is represented in light gray. The red dots represent cases with one unstable FM mode. The green dots represent cases with one unstable FM mode plus one unstable EM mode. The orange dots represent cases with one unstable EM mode. The black dots represent cases without any unstable mode(s). (**b**) The amplitude of vibration as a function of U^*. The boundary lines in (**a**) and response curves in (**b**) are re-plotted by using digitized data extracted from Bourguet & Lo Jacono [9].

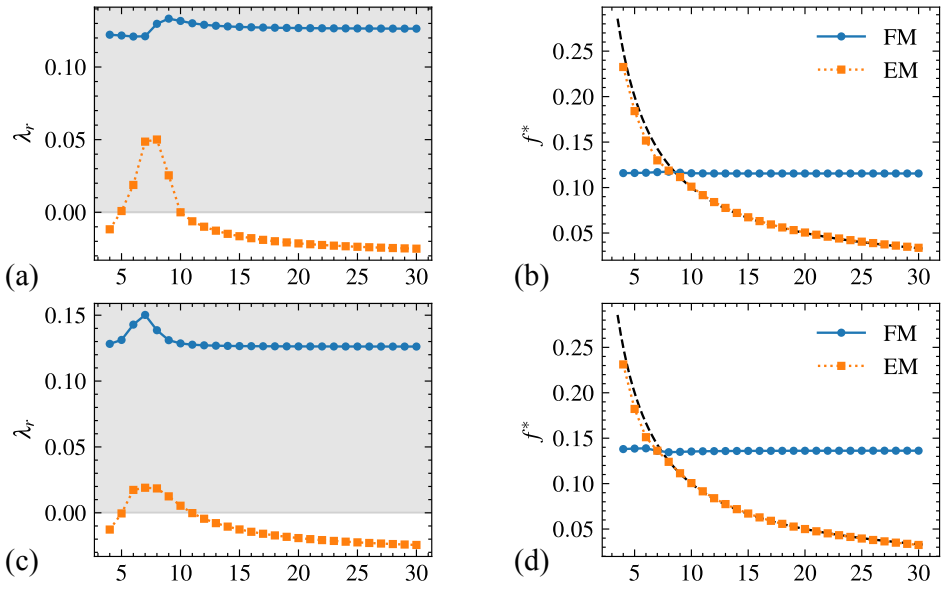

Figure 6. *Cont.*

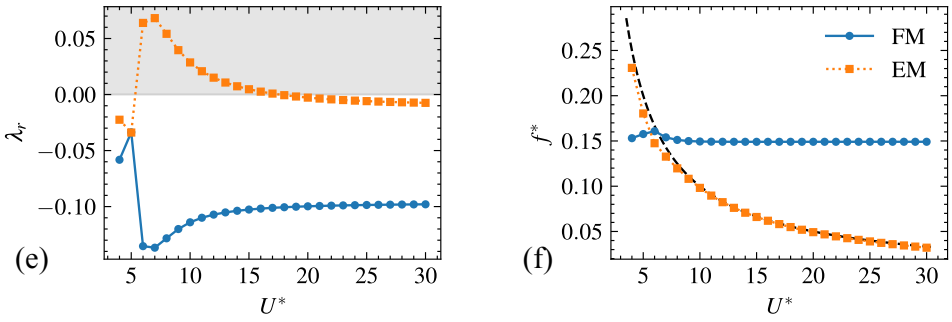

Figure 6. LSA results for the FIV of a cross-flow oscillator at $Re = 100$ (series 2): growth gate λ_r and dimensionless frequency $f^* = \lambda_i/(2\pi)$ as a function of U^* at $\alpha = 0$ (**a**,**b**); $\alpha = 1.0$ (**c**,**d**); $\alpha = 2.0$ (**e**,**f**). The unstable regions (with a positive growth gate) in the (**left panel**) are shaded in gray. The (dimensionless) natural frequencies ($f_n = 1/U^*$) as a function of U^* are shown as dashed lines in the **(right panel)**.

Figure 7 shows the structures of the FM and EM modes for some cases at $\alpha = 1.0$ and $\alpha = 3.0$. Similar to the those in series 1, the structures of FM modes are not affected by varying U^*, while the structures of EM modes strongly depend on the value of U^*.

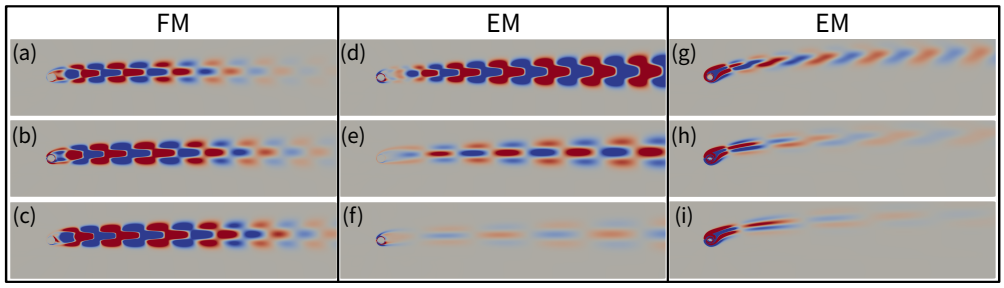

Figure 7. Mode structures for some cases in series 2: vorticity fields of FM mode (**left panel**) and EM mode (**middle panel**) for $\alpha = 1.0$, and EM mode for $\alpha = 3.0$ (**right panel**). Frames (**a**,**d**,**g**), (**b**,**e**,**h**), and (**c**,**f**,**i**) are calculated for $U^* = 6.0, 10.0, 15.0$, respectively. The ranges of vorticity are $[-10^{-3}, 10^{-3}]$ for (**a**–**f**), and $[-5 \times 10^{-6}, 5 \times 10^{-6}]$ for (**g**–**i**). The incoming flow is from left to right.

4.4. 2-DOF Oscillation at a Supercritical Reynolds Number (Series 3)

Some results for series 3 from the nonlinear simulation of Bourguet [12] are summarized in Figure 8. Figure 8a shows the vibration and non-vibration regions in the space of (U^*, α). In comparison with that for series 2, the area of vibration region expands significantly and covers almost the entire parameter space. The cases selected for conducting LSA are denoted as dots with different colors, depending on stability properties of the leading modes. It is seen that the boundary lines between different regions in Figure 8a can be predicted by using stability properties of the leading modes. Figure 8b shows the amplitude of oscillation as a function of U^* at various α. At $\alpha = 0$ and $\alpha = 1.0$, the response curves are bell-shaped and similar to those observed in series 2 at the same values of α. The curves of this type is also a hallmark of VIV response. At $\alpha = 2.0$, the response curve is sawtooth-shaped. This type of curve is seldomly seen and can be regarded as abnormal behavior of such FIV system. At $\alpha = 3.0$ and $\alpha = 4.0$, the response curves are qualitatively similar to those in series 1 at the high range of α. The amplitudes at these two values of α increase unboundedly with increasing U^*, exhibiting the typical behavior of galloping.

Figure 9 shows the variations in growth rate (λ_r) and non-dimensional frequency (f^*) with U^* for the leading modes calculated at $\alpha = 0, 1.0, 2.1, 3.0$. At $\alpha = 0$, similar to series 2, the FM mode is found to be unstable in the entire range of U^*, and the EM mode is found to be unstable in a narrow range of $5.0 \leq U^* \leq 10.0$. This range of U^* (where two unstable modes co-exist) roughly coincides with that for the high-amplitude VIV-type

response shown in Figure 8b. At $\alpha = 1.0$, the stability properties of the leading modes are very similar to those for $\alpha = 0$. The FM mode remains consistently unstable, while the unstable range of U^* for the EM mode slightly narrows. At $\alpha = 2.1$, similar to the situations in series 1 and series 2, the FM mode is stabilized in the entire range of U^*. The EM mode now becomes unstable in a relatively wide range of $4.5 \leq U^* \leq 22.0$. At $\alpha = 3.0$, the unstable range of the EM mode further expands and covers the high limit of U^*. Overall, the stability properties of the leading modes for series 3 show some similarities with those for series 2 at the low range of α, while resemble those for series 1 at the high range of α. There are some additional remarks regarding stability properties of the leading modes for $1.8 \leq \alpha \leq 2.0$. The curves of growth rate and frequency of the leading modes resemble those for $\alpha = 2.1$ (not shown here for brevity). In other words, the complex geometry of the boundary line between vibration and non-vibration regions and abnormal behavior in the response curve shown in Figure 8 cannot be interpreted by LSA results.

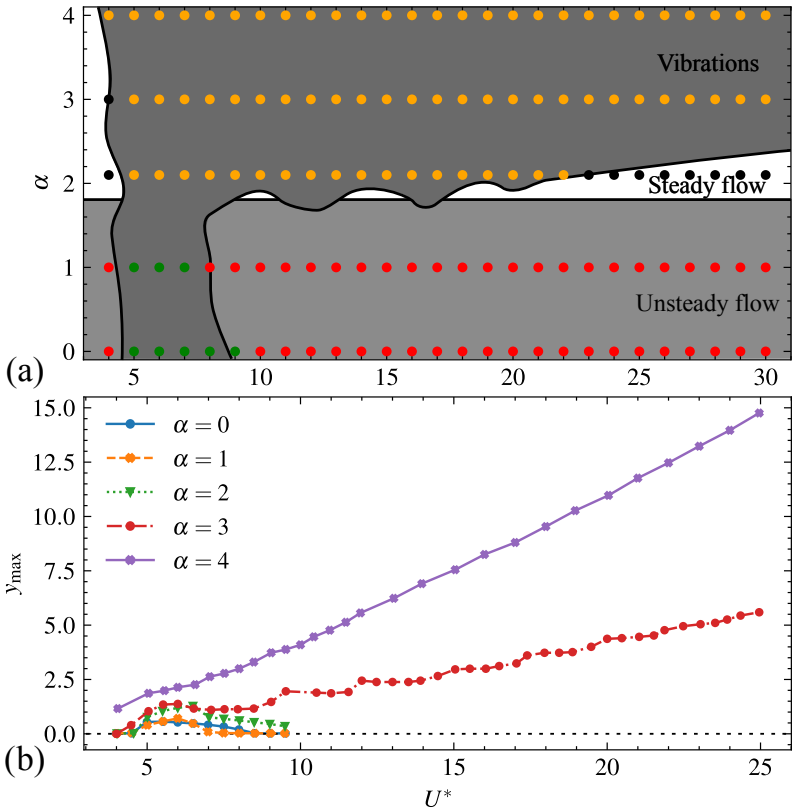

Figure 8. Results from nonlinear simulation for the FIV of a 2-DOF oscillator at $Re = 100$ (series 3): (**a**) vibration region and non-vibration region in space of (U^*, α). The vibration region where the (cross-flow) amplitude of oscillation is larger than 0.03D is represented in dark gray. The vibration region with small amplitude of oscillation (and flow unsteadiness) is represented in light gray. The black dots represent cases without unstable modes. The red and orange dots represent cases with one unstable FM mode and one unstable EM mode, respectively. The green dots represents cases with two unstable modes (one FM mode plus one EM mode). (**b**) amplitude of (cross-flow) oscillation as a function of U^*. The boundary lines in (**a**) and response curves in (**b**) are re-plotted by using digitized data extracted from Bourguet [12].

The structures of modes for some cases at $\alpha = 1$ and $\alpha = 3$ are shown in Figure 10. Similar to the other two series above, the structures of the EM modes are modified obviously by varying U^*, the influence of U^* on the structures of the FM modes is much smaller.

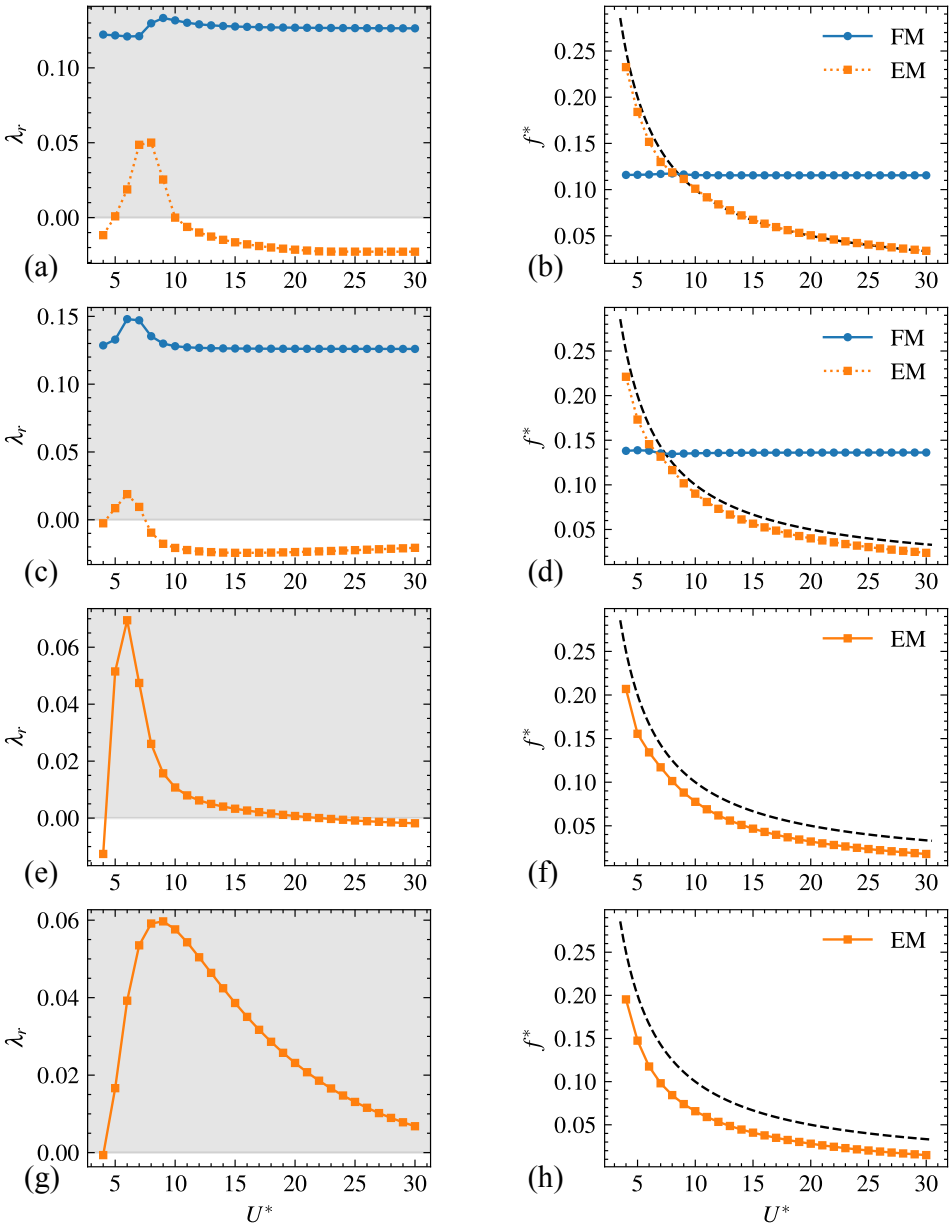

Figure 9. LSA results for the FIV of a 2-DOF oscillator at $Re = 100$ (series 3): growth gate λ_r and dimensionless frequency $f^* = \lambda_i/(2\pi)$ as a function of U^* at $\alpha = 0$ (**a**,**b**); $\alpha = 1.0$ (**c**,**d**); $\alpha = 2.1$ (**e**,**f**); $\alpha = 3.0$ (**g**,**h**). The unstable regions (with a positive growth gate) in the (**left panel**) are shaded in gray. The (dimensionless) natural frequencies ($f_n = 1/U^*$) as a function of U^* are shown as dashed lines in the (**right panel**).

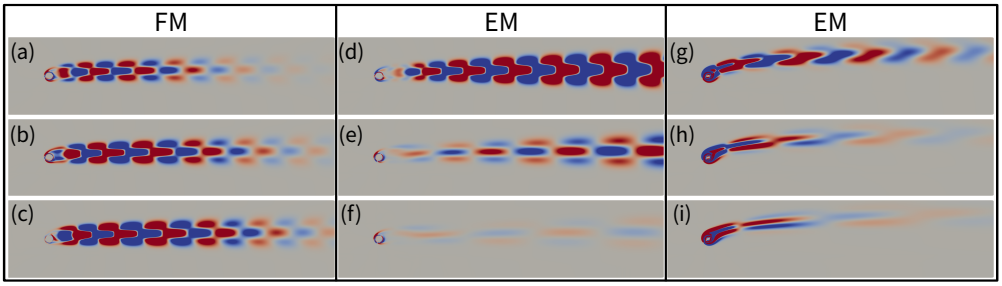

Figure 10. Mode structures for some cases in series 3: vorticity fields of FM mode (**left panel**) and EM mode (**middle panel**) for $\alpha = 1$, and EM mode for $\alpha = 3$ (**right panel**). Frames (**a**,**d**,**g**), (**b**,**e**,**h**), and (**c**,**f**,**i**) are calculated for $U^* = 6, 10, 15$, respectively. The range of vorticity is $[-10^{-3}, 10^{-3}]$ for (**a**–**f**), and $[-5 \times 10^{-6}, 5 \times 10^{-6}]$ for (**g**–**i**). The incoming flow is from left to right.

4.5. 2-DOF Oscillation at a Subcritical Reynolds Number (Series 4)

Some results for series 4 from the nonlinear simulation of Bourguet [15] are summarized in Figure 11. Figure 11a shows the vibration and non-vibration regions in the space of (U^*, α). Unlike the other three series, the region of small-amplitude vibration (with flow unsteadiness) disappears. The vibration region extends from $\alpha = 0$ to $\alpha = 4.0$. The range of U^* for the vibration region first narrows and then widens with increasing α. The narrow-necked place is found to be located at $\alpha = 1.0$. The cases selected for conducting LSA are denoted by dots in different colors, depending on stability properties of the leading modes. It is seen that the boundary lines between the vibration and non-vibration regions can be predicted by using stability properties of the leading modes. Figure 11b shows the amplitudes of oscillation as a function of U^* at various α. At $\alpha = 0, 1.0, 2.0$, the response curves are bell-shaped and of VIV type. At $\alpha = 3.0$, the amplitude of oscillation is much higher than those at $\alpha = 0, 1.0, 2.0$. It first increases monotonically with U^* and reaches a peak amplitude of $3.5D$ at $U^* = 25.0$. The amplitude then decreases steeply with increasing U^* and becomes zero for $U^* > 28.0$. At $\alpha = 4.0$, the amplitude increases unboundedly with increasing U^*. The oscillation amplitude reaches a value as high as $10D$ at the high limit of U^*. This galloping-like response curve looks similar to that observed in series 3 at the same value of α.

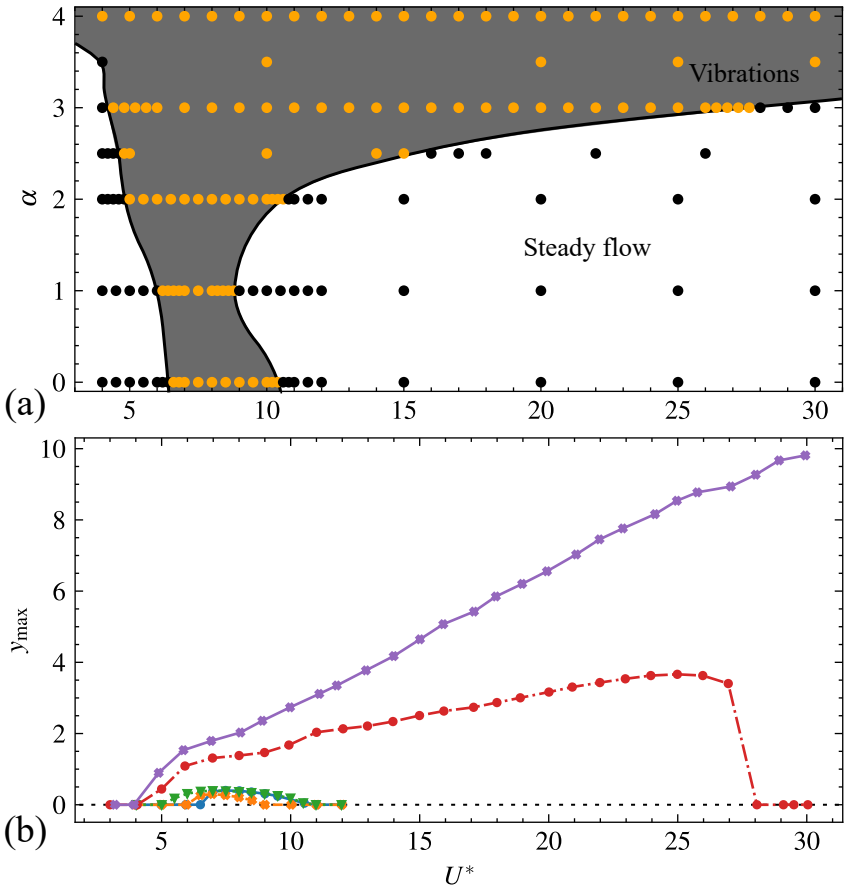

Figure 11. Results from nonlinear simulation for the FIV of a 2-DOF oscillator at $Re = 30$ (series 4): (**a**) vibration region and non-vibration region in space of (U^*, α). The vibration region is represented in dark gray. The black dots represent cases without unstable mode(s). The orange dots represent cases with one unstable EM mode. (**b**) cross-flow oscillation amplitude as a function of U^* at various values of α. The boundary lines in (**a**) and response curves in (**b**) are re-plotted by using digitized data extracted from Bourguet [15].

Figure 12 shows the variation in λ_r and f^* with U^* for the leading modes calculated for $\alpha = 0, 1.0, 3.0, 4.0$. It is seen that, at a subcritical Reynolds number, no unstable FM mode can be found, while the EM mode is unstable in certain range of U^*. The unstable range of the EM mode first reduces and then increases with increasing α. At low rotation rates, the unstable ranges for the EM mode are relatively narrow. More specifically, the ranges are $6.4 < U^* < 10.6$ and $6.0 < U^* < 9.0$ at $\alpha = 0$ and $\alpha = 1.0$, respectively. At $\alpha = 3.0$, a much wider unstable range of $4.5 < U^* < 27.8$ for the EM mode can be identified. At $\alpha = 4.0$, the unstable range is found to be the entire range of U^*. The unstable ranges of U^* at different values of α are found to be consistent with those for the vibration region shown in Figure 11a.

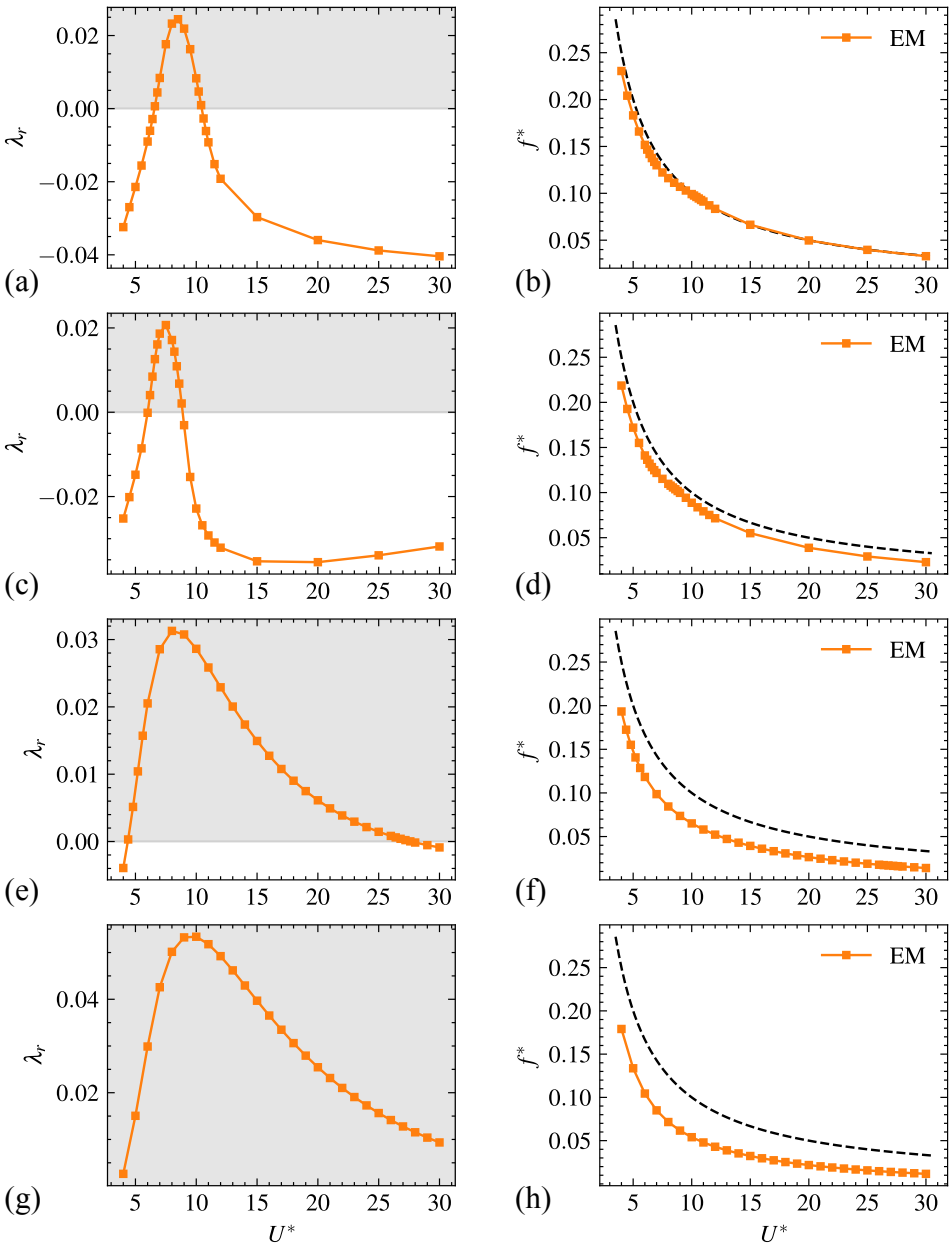

Figure 12. LSA results for FIV of a 2-DOF oscillator at $Re = 30$ (series 4): growth gate λ_r and dimensionless frequency $f^* = \lambda_i/(2\pi)$ as a function of U^* at $\alpha = 0$ (**a**,**b**); $\alpha = 1.0$ (**c**,**d**); $\alpha = 3.0$ (**e**,**f**); $\alpha = 4$ (**g**,**h**). The unstable regions (with a positive growth gate) in the (**left panel**) are shaded in gray. The (dimensionless) natural frequencies ($f_n = 1/U^*$) as a function of U^* are shown as dashed lines in the (**right panel**).

The structures of the EM modes for some cases at $\alpha = 1.0$ and $\alpha = 3.0$ are shown in Figure 13. The dependency of mode structures on U^* resembles the scenarios of other three series.

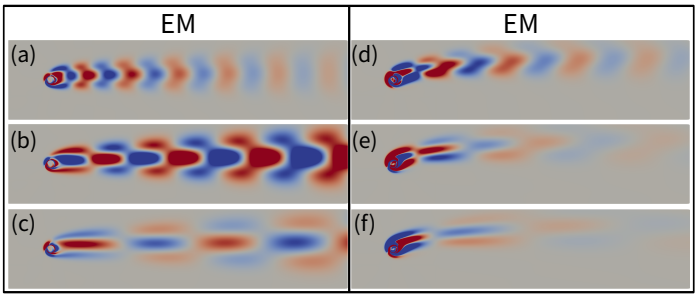

Figure 13. Mode structures for some cases in series 4: vorticity fields of EM modes at $\alpha = 1.0$ (**left panel**) and $\alpha = 3.0$ (**right panel**). Frames (**a**,**d**), (**b**,**e**) and (**c**,**f**) are for $U^* = 6.0, 10.0, 15.0$, respectively. The ranges of vorticity are $[-5 \times 10^{-5},\ 5 \times 10^{-5}]$ for frames (**a**–**c**), $[-5 \times 10^{-6},\ 5 \times 10^{-6}]$ for frames (**d**–**f**). The incoming flow is from left to right.

5. Conclusions

The flow-induced vibration of an elastically mounted rotating cylinder was investigated by using LSA. Four series of cases with different combinations of degrees of freedom in oscillation and Reynolds number are considered. For each series, a wide range of reduced velocity $U^* \in [4.0,\ 30.0]$ and rotation rate $\alpha \in [0,\ 4.0]$ was explored. The growth rates and frequencies of the leading modes as a function of reduced velocity are presented. The impact of forced rotation on FIV behaviors of the system has been interpreted by examining its influence on stability properties of the leading modes, and some new insights have been gained.

At a supercritical Reynolds number, an unstable FM mode can always be identified in the non-rotating case. The instability of the EM mode may exist or not, depending on the degrees of freedom of the oscillation. The FIV behavior of the system strongly depends on the stability properties of the FM and EM modes. The coexistence of two unstable modes in a certain range of the reduced velocity is associated with the resonance (synchronization) mechanism which leads to VIV.

In the low range of rotation rate, the imposed rotation barely affects stability properties of the FM and EM modes. Thus, the FIV behavior is similar to that of the non-rotating case. In the intermediate and high ranges of rotation rate, the imposed rotation tends to stabilize the FM mode. Thus, the FIV behavior only depends on stability properties of the EM mode. In the absence of unstable EM mode, the cylinder vibration and flow unsteadiness are completely inhibited. The existence of an unstable EM mode in certain range of reduced velocity is correlated with high-amplitude oscillation observed in nonlinear simulation. An expanded unstable range of the EM mode which covers the high limit of reduced velocity is correlated with galloping-like response observed in nonlinear simulation.

At a subcritical Reynolds number, only one unstable EM mode can be identified in the case of 2-DOF oscillation. When the rotation rate increases, the unstable range of the EM mode first decreases and then increases. This explains why the range of reduced velocity for high-amplitude oscillation in nonlinear simulation first narrows and then widens with increasing rotation rate. In the high range of rotation rate, the EM mode is found to be unstable in the entire range of reduced velocity. This is correlated with galloping-like responses observed in nonlinear simulation.

The limitations of LSA also merit further discussion. We found that some phenomena observed in nonlinear simulation cannot be interpreted by using LSA results. One example is the modification of wake topology by imposed rotation and the formation of different

wake patterns at various rotation rates. The reason behind this is that the evolution of wake strongly depends on the nonlinear effect inherited in Navier–Stokes equations, while such effect is not taken into account in LSA.

Author Contributions: Conceptualization, J.L., Z.Z., and X.Z.; methodology, J.L., Z.Z., and X.Z.; validation, J.L.; formal analysis, J.L.; investigation J.L., X.Z., and Z.Z.; writing—original draft preparation, J.L. and X.Z.; writing—review and editing, J.L. and X.Z.; supervision, X.Z.; funding acquisition, X.Z. All authors have read and agreed to the published version of the manuscript.

Funding: This research was funded by the National Natural Science Foundation of China grant numbers 11372331, 11772338, 12172361, and the Chinese Academy Sciences grant numbers XDB22040104 and XDA22040203. This research was also supported by the "Open fund of State Key Laboratory of Hydraulic Engineering Intelligent Construction and Operation", Tianjin University.

Data Availability Statement: The raw data supporting the conclusions of this article will be made available by the authors on request.

Conflicts of Interest: The authors declare no conflicts of interest.

Appendix A. Mesh and Domain Independence Tests

In the mesh independence test, a series of stretched Cartesian meshes are used. 2-DOF oscillation with the control parameters of $(Re = 30, M^* = 10, \alpha = 2, U^* = 10.)$ is the testing case. Three different mesh resolutions are employed, with the finest grid spacing near the cylinder being $D/25$, $D/50$ and $D/100$, respectively. The effect of grid spacing on eigenvalues is shown in Table A1. The result indicates that the grid spacing of $D/50$ is fine enough for obtaining accurate eigenvalues.

Table A1. Effect of mesh resolution on eigenvalues of two leading modes.

Grid Spacing	$\Delta x = D/25$	$\Delta x = D/50$	$\Delta x = D/100$
FM	−0.0237 + 0.5572i	−0.0229 + 0.5574i	−0.0223 + 0.5575i
EM	−0.0454 + 0.6438i	−0.0457 + 0.6424i	−0.0459 + 0.6417i

A domain-size independence test is also conducted on the same case. From Table A2, it is observed that a domain size of $[80D \times 56D]$ is sufficiently large for obtaining accurate eigenvalues.

Table A2. Effect of domain size on eigenvalues of two leading modes.

Domain Size	$[56D \times 40D]$	$[80D \times 56D]$	$[104D \times 74D]$
FM	−0.0237 + 0.5546i	−0.0229 + 0.5574i	−0.0235 + 0.5587i
EM	−0.0447 + 0.6412i	−0.0457 + 0.6424i	−0.0452 + 0.6433i

References

1. Williamson, C.H.K.; Govardhan, R. Vortex-induced vibrations. *Annu. Rev. Fluid Mech.* **2004**, *36*, 413–455. [CrossRef]
2. Wang, J.L.; Geng, L.F.; Ding, L.; Zhu, H.J.; Yurchenko, D. The state-of-art review on energy harvesting from flow-induced vibrations. *Appl. Energy* **2020**, *267*, 114902. [CrossRef]
3. Blevins, R.D. *Flow-Induced Vibration*; Van Nostrand Reinhold Company: New York, NY, USA, 1977.
4. Mittal, S.; Singh, S. Vortex-induced vibrations at subcritical *Re*. *J. Fluid Mech.* **2005**, *534*, 185–194. [CrossRef]
5. Munir, A.; Zhao, M.; Wu, H.; Tong, F. Flow-induced vibration of a rotating circular cylinder at high reduced velocities and high rotation rates. *Ocean Eng.* **2021**, *238*, 109562. [CrossRef]
6. Wong, K.W.L.; Zhao, J.; Lo Jacono, D.; Thompson, M.C.; Sheridan, J. Experimental investigation of flow-induced vibration of a rotating circular cylinder. *J. Fluid Mech.* **2017**, *829*, 486–511. [CrossRef]
7. Seyed-Aghazadeh, B.; Modarres-Sadeghi, Y. An experimental investigation of vortex-induced vibration of a rotating circular cylinder in the cross-flow direction. *Phys. Fluids* **2015**, *27*, 067101. [CrossRef]

8. Zhao, M.; Cheng, L.; Lu, L. Vortex-induced vibrations of a rotating circular cylinder at low Reynolds Number. *Phys. Fluids* **2014**, *26*, 073602. [CrossRef]
9. Bourguet, R.; Lo Jacono, D. Flow-induced vibrations of a rotating cylinder. *J. Fluid Mech.* **2014**, *740*, 342–380. [CrossRef]
10. Bourguet, R.; Lo Jacono, D. In-line flow-induced vibrations of a rotating cylinder. *J. Fluid Mech.* **2015**, *781*, 127–165. [CrossRef]
11. Bourguet, R. Flow-induced vibrations of a rotating cylinder in an arbitrary direction. *J. Fluid Mech.* **2019**, *860*, 739–766. [CrossRef]
12. Bourguet, R. Two-degree-of-freedom flow-induced vibrations of a rotating cylinder. *J. Fluid Mech.* **2020**, *897*, A31. [CrossRef]
13. Sahu, T.R.; Navrose; Mittal, S. Multiple regimes of lock-in and hysteresis in free vibration of a rotating cylinder. *Phys. Fluids* **2023**, *35*, 123606. [CrossRef]
14. Amini, Y.; Zahed, I.; Mahini, M.; Izadpanah, E. Effects of mass ratio and rotation speed on flow-induced vibration of a rotating cylinder with two degrees of freedom. *Phys. Fluids* **2024**, *36*, 087112. [CrossRef]
15. Bourguet, R. Forced rotation enhances cylinder flow-Induced vibrations at subcritical Reynolds Number. *J. Fluid Mech.* **2023**, *955*, R3. [CrossRef]
16. Zhang, Z.Y.; Lu, J.F.; Zhang, X. Global stability analysis of flow-induced-vibration problems using an immersed boundary method. *J. Fluids Struct.* **2024**, *130*, 104187. [CrossRef]
17. Wang, S.Z.; Zhang, X. An immersed boundary method based on discrete stream-function formulation for two- and three-dimensional incompressible flows. *J. Comput. Phys.* **2011**, *230*, 3479–3499. [CrossRef]